Biogeosciences

Detection and spatiotemporal analysis of methane ebullition on thermokarst lake ice using high-resolution optical aerial imagery

P. R. Lindgren[1], **G. Grosse**[1,2], **K. M. Walter Anthony**[3], and **F. J. Meyer**[1]

[1]Geophysical Institute, University of Alaska Fairbanks, Fairbanks, USA
[2]Alfred Wegener Institute Helmholtz Centre for Polar and Marine Research, Potsdam, Germany
[3]Water and Environmental Research Center, University of Alaska Fairbanks, Fairbanks, USA

Correspondence to: P. R. Lindgren (pregmi@alaska.edu)

Abstract. Thermokarst lakes are important emitters of methane, a potent greenhouse gas. However, accurate estimation of methane flux from thermokarst lakes is difficult due to their remoteness and observational challenges associated with the heterogeneous nature of ebullition. We used high-resolution (9–11 cm) snow-free aerial images of an interior Alaskan thermokarst lake acquired 2 and 4 days following freeze-up in 2011 and 2012, respectively, to detect and characterize methane ebullition seeps and to estimate whole-lake ebullition. Bubbles impeded by the lake ice sheet form distinct white patches as a function of bubbling when lake ice grows downward and around them, trapping the gas in the ice. Our aerial imagery thus captured a snapshot of bubbles trapped in lake ice during the ebullition events that occurred before the image acquisition. Image analysis showed that low-flux A- and B-type seeps are associated with low brightness patches and are statistically distinct from high-flux C-type and hotspot seeps associated with high brightness patches. Mean whole-lake ebullition based on optical image analysis in combination with bubble-trap flux measurements was estimated to be 174 ± 28 and $216 \pm 33 \, \mathrm{mL \, gas \, m^{-2} \, d^{-1}}$ for the years 2011 and 2012, respectively. A large number of seeps demonstrated spatiotemporal stability over our 2-year study period. A strong inverse exponential relationship ($R^2 \geq 0.79$) was found between the percent of the surface area of lake ice covered with bubble patches and distance from the active thermokarst lake margin. Even though the narrow timing of optical image acquisition is a critical factor, with respect to both atmospheric pressure changes and snow/no-snow conditions during early lake freeze-up, our study shows that optical remote sensing is a powerful tool to map ebullition seeps on lake ice, to identify their relative strength of ebullition, and to assess their spatiotemporal variability.

1 Introduction

Soils in the northern permafrost region contain 1300–1370 Pg organic carbon with an uncertainty range of 930–1690 Pg (Hugelius et al., 2014). A large amount of soil carbon in the Yedoma permafrost region (~ 450 Pg) is found in thick Holocene deposits in thermokarst lakes and basins, undisturbed Pleistocene-age ice-rich silts known as yedoma, and Pleistocene deposits which have thawed underneath lakes and later refrozen (Grosse et al., 2011; Walter Anthony et al., 2014). However, permafrost degradation can facilitate the transfer of this permafrost-stored carbon to the atmosphere in the form of the greenhouse gases carbon dioxide (CO_2) and methane (CH_4), resulting in a positive feedback to global climate change (Zimov et al., 2006; Walter et al., 2006; Schuur et al., 2008; Koven et al., 2011). One common and effective form of permafrost degradation involves formation and growth of thermokarst lakes (Grosse et al., 2013; Kokelj and Jorgenson, 2013), which tap into deep (up to 60 m) permafrost carbon pools (Zimov et al., 1997; Walter et al., 2008).

Thermokarst lakes are a prominent landscape feature in the high northern latitudes (Smith et al., 2007; Grosse et al., 2013). They are formed in closed depressions following the thawing of ice-rich permafrost or melting of massive ice. Once initiated, the presence of a water body on permafrost serves as a positive feedback to permafrost degradation. Depending on the amount of excess ice content in permafrost, this positive feedback accelerates the growth of thermokarst lakes in both lateral and vertical directions (Jorgenson and Shur, 2007; Plug and West, 2009; Kokelj and Jorgenson, 2013). Over many years, taliks (thaw bulbs) of perennially thawed soil develop beneath thermokarst lakes (Hinzman et al., 2005; West and Plug, 2008; Rowland et al., 2011), creating conditions favorable for year-round methane production through anaerobic decomposition of organic matter by microbes (Zimov et al., 1997; Walter et al., 2006, 2008; Kessler et al., 2012). During lateral expansion, thermal erosion along the lake margin also releases both Holocene and Pleistocene organic matter from adjacent soils into anaerobic lake bottoms, further enhancing methanogenesis (Zimov et al., 1997; Walter Anthony et al., 2014).

Ebullition (bubbling) is considered the dominant pathway of methane release from lakes to the atmosphere (Keller and Stallard, 1994; Bastviken et al., 2011). Methane produced in dense lake sediments and thaw bulbs emerges primarily through intrasedimentary bubble tubes as point-source seeps on the lake bed (Walter Anthony et al., 2010). In the high northern latitude region, where lake surfaces freeze throughout the winter, most bubbles emerging from the lake bed ascend through the water column and get trapped by ice as gas pockets (Walter et al., 2008; Greene et al., 2014). Ongoing ice growth can separate ice-trapped bubbles from an individual seep by thin films of ice, resulting in vertically oriented bubble columns in the ice. Walter et al. (2006) took advantage of this phenomenon to reveal locations and relative strength of point sources of methane seep ebullition across lake ice. They identified four major types of methane ebullition seeps based on ice-bubble cluster morphology and they measured daily mean ebullition rates (mean ± standard error of mean) (Fig. 1) (Walter Anthony and Anthony, 2013). It should be noted that the seep class-specific ebullition rates reported represent the daily average of thousands of flux measurements, measured on 24 pan-Arctic lakes in continuous and discontinuous permafrost regions for up to 700 days; however, bubbling within each class is highly episodic, and bubbling rates of individual seeps are not constant over time (Walter Anthony et al., 2010; Walter Anthony and Anthony, 2013): (1) A-type seeps are characterized by isolated bubbles stacked in multiple vertical layers with less than 50 % of all gas volume merged in bubble clusters. A-type seeps have the lowest ebullition rate (22 ± 4 mL gas d^{-1}); (2) B-type seeps are dominated by laterally merged bubbles stacked in multiple layers (more than 50 % of all gas volume merged in a bubble cluster). The ebullition rate of this bubble type is 211 ± 39 mL gas d^{-1}; (3) C-type seeps, associated with an

ebullition rate of 1726 ± 685 mL gas d^{-1}, are characterized by single large gas pockets (usually > 40 cm in diameter) separated vertically by ice layers containing few or no bubbles; and (4) hotspot seeps have the highest ebullition rate, on average 7801 ± 764 mL gas d^{-1}. Due to upwelling of water associated with frequent bubble streams, hotspots generally appear as open water holes in lake ice following freeze-up. Usually a thin snow–ice film develops over hotspots in winter, visually masking them at the surface; however, ice blocks cut from the lake throughout winter and spring reveal that hotspot bubbling maintains a large ice-free cavity throughout winter (Greene et al., 2014).

Accounting for methane ebullition from northern thermokarst lakes can significantly improve estimates of lake contributions to regional and global atmospheric carbon budgets (Walter et al., 2007; Bastviken et al., 2011). However, due to challenges associated with the logistics of fieldwork in remote locations as well as spatial and temporal heterogeneity of ebullition, accurate estimation of methane flux from thermokarst lakes is difficult (Casper et al., 2000; Bastviken, 2004; Wik et al., 2011). Most studies have been carried out using field measurements to understand the spatial and temporal variability of methane ebullition. However, the insufficiency of field data is a recurring issue since it is difficult to sample the entire lake area, particularly when lakes have remote locations. This may lead to an unrealistic characterization of variability of ebullition bubbles and a less accurate estimation of methane flux at a regional scale. Recently, Walter Anthony and Anthony (2013) combined point-process modeling with field-measured data to understand the drivers of ebullition spatial variability in thermokarst lakes and provided ways to reduce uncertainty in regional-scale lake ebullition estimates based on limited field data; nonetheless spatially limited field sampling remains a hindrance to whole-lake ebullition quantification.

Remote sensing methods combined with field observations can help overcome some of the limitations that exist in a sole field-survey method. One of the major advantages of remote sensing tools is that they may provide the possibility to map the entire population of methane ebullition bubbles on a lake. Moreover, remote sensing can overcome the logistical difficulties that exist in accessing methane-bubbling lakes in the remote regions of the Arctic and Subarctic. Walter et al. (2008) and Engram et al. (2012) demonstrated the potential application of synthetic aperture radar (SAR) satellite imagery to estimate whole-lake ebullition from spatially limited field measurements of ebullition along survey transects. These studies showed correlation of radar backscatter values with the percent of the surface area of lake ice covered with bubbles and field-measured methane ebullition rates based on bubble-trap measurements from lakes. Additionally, Walter Anthony et al. (2012) used aerial surveys to identify, photograph, and map large (~ 1 to > 300 m^2) bubbling-induced open water holes in ice-covered lakes in
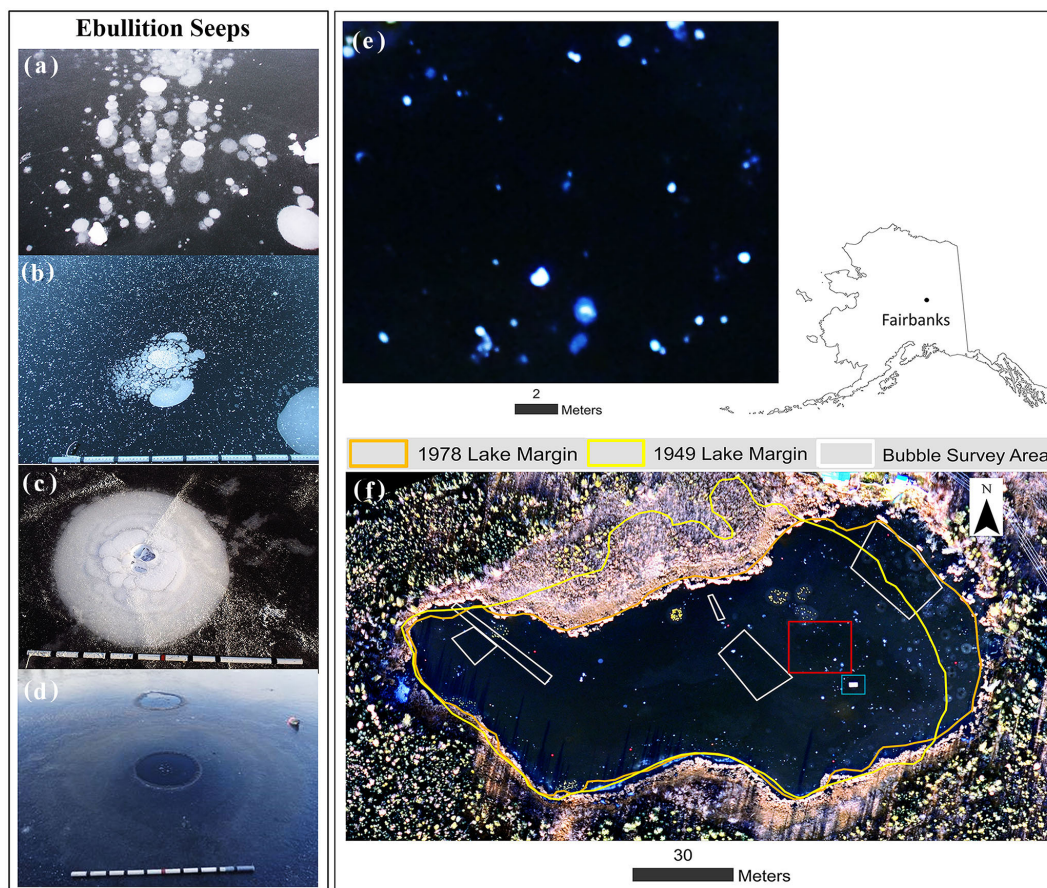
Figure 1. Photos show four distinct patterns of point-source ebullition seeps in early winter lake ice: **(a)** A-type; **(b)** B-type; **(c)** C-type; **(d)** hotspot. The white speckles on the background lake ice surface in **(b)** are snow/hoar ice crystals, not bubbles; **(e)** a close-up (red box in the lake image shown in **(f)**) shows the appearance of ebullition bubble patches as bright white spots on the aerial image (natural color composite of red, green, and blue bands) of Goldstream Lake (64.91° N, 147.84° W), Fairbanks, Alaska, acquired on 14 October 2011. A rectangular wooden instrument platform (highlighted by the blue box) also appears bright.

Alaska associated with geologic methane seepage. Geologic methane seeps differ distinctly from ecological seeps in associated fluxes (i.e., fluxes of geologic seeps are several orders of magnitude higher than for ecological seeps) and their spatial distribution is often aligned with geological faults. Coupling aerial surveys with ground truth flux measurements and laboratory analyses, this study showed that geologic methane seepage is not extensive, but it is important in some regions of Alaska underlain by leaky hydrocarbon reservoirs.

Since open holes induced by bubbling in snow-covered lake ice are visually distinct, and since lower-flux ebullition bubble clusters trapped inside ice appear as bright white features that have a strong contrast against dark, bubble-, and snow-free congelation ice (Fig. 1), there is the potential and need to detect and quantify methane bubbles with optical remote sensing. In this study, we explored high-resolution optical remote sensing images to characterize methane ebullition seeps on Goldstream Lake, an interior Alaska thermokarst lake, and to study their spatiotemporal dynamics.

2   Study site

Goldstream Lake (64.91° N, 147.84° W; 195 m a.s.l.) is an interior Alaska thermokarst lake covering an area of approximately $10\,300\,\mathrm{m}^2$ with maximum and average depths of 2.9 and 1.6 m, respectively. The lake formed in "yedoma-type" deposits of retransported late Quaternary loess at the toe slope of Goldstream Valley in Fairbanks (Péwé, 1975; Kanevskiy et al., 2011; Walter Anthony and Anthony, 2013). Based on remotely sensed aerial and satellite images, the lake partially drained between 1949 and 1978 but has been expanding mainly along the eastern shore since then (Fig. 1f). This active thermokarst expansion is also indicated by spruce trees leaning lakeward along the eastern lake margin, and standing dead trees submerged in the lake offshore of the eastern margin. The vegetation around the lake is dominated by black spruce and willow. Cattail (*Typha* spp.) grows along some shallow margins of the lake. Water lilies (*Nuphar* spp.)

are also found in several locations on the northern and south-western parts of the lake.

Ebullition accounts for a total of 83 % of methane emission from Goldstream Lake (Greene et al., 2014). The concentration of methane in Goldstream Lake's bubbles is 82–89 % (Greene et al., 2014). Ice formation on the lake usually occurs between the end of September and mid-October, reaches maximum thickness by mid-March, and ice break-up occurs around the end of April or early May. Vertically oriented layers of methane ebullition bubbles (Fig. 1), representing point-source seeps, are widespread in the lake ice, particularly along the eastern margin (Walter Anthony and Anthony, 2013). Many hotspot seeps are also found near the eastern eroding shore and are seen as open holes in lake ice during early winter and spring.

3　Methods

We used three sets of data in our study: (1) high-resolution snow-free early winter lake ice images from fall 2011 and 2012, (2) high-resolution snow-covered early winter lake images from fall 2012, and (3) field-based surveys of ebullition bubble seep types and their fluxes.

We first processed the aerial images of snow-free early winter lake ice acquired in the fall of 2011 and 2012 and then mapped ebullition bubbles trapped in the ice. We refer to the bubble features seen in our snow-free images as "bubble patches" henceforth since the image resolution was not sufficient to fully resolve smaller individual bubbles (Fig. 1). Then we characterized imaged bubble patches based on field-collected ebullition bubble seep data collected approximately 1–2 weeks after image acquisition when ice was safe to walk on in the fall of 2011 and 2012 and again in spring of the following year. We hypothesized that the brightness of bubble patches correlates with the strength of methane flux associated with four classes of ebullition bubble seeps (A, B, C, and hotspot) identified by Walter Anthony et al. (2010). We estimated from aerial photos the bubble-patch density for each seep class and the mean whole-lake seep ebullition. Finally, we examined the spatial patterns of seep locations in the lake with respect to eroding thermokarst shores, and analyzed interannual variability of seep occurrences by comparing imagery from different years.

Due to similar spectral characteristics of open water and dark lake ice, open-hole hotspots are difficult to map on snow-free lake ice images; but they are easily identifiable on snow-covered lake ice images. Therefore, we also collected high-resolution snow-covered aerial images in the fall of 2012 to map open-hole hotspots on the lake. We compared the locations of hotspots in aerial images with maps of hotspot locations determined by field measurements over multiple years to assess hotspot regularity.

3.1　Remotely sensed high-resolution image acquisition

We scheduled low-altitude, high-resolution aerial image acquisitions to map and characterize methane ebullition bubble patches (A, B, C, and ice-covered hotspots) during a narrow time window in the early winter, when first ice had formed but was still snow-free. Images were acquired in nadir with a Navion L17a plane using a Nikon D300 camera system mounted in a belly port on 14 October 2011 and 13 October 2012, 2 and 4 days following freeze-up, respectively. Flight altitude for the acquisitions was ∼ 750 m a.s.l. in 2011 and ∼ 587 m a.s.l. in 2012. Image scale was 1 : 20 000 and 1 : 17 000 for 2011 and 2012, respectively, which in turn corresponds to ground sampling distances (GSD) of 11 and 9 cm.

We collected images of the snow-covered lake in fall 14 October 2012 using an unmanned aerial vehicle (UAV) mounted with an Aptina MT9P031 board camera to map open-hole hotspot seep locations. The images were acquired from a flying height of approximately 230 m a.s.l., corresponding to an image scale 1 : 30 000 and GSD of 6 cm. All the images consisted of three visible bands: red, green, and blue (RGB).

3.2　Ground truth field data

We collected the point location data of (1) the lake perimeter and permanently installed reference markers as ground control points (GCPs) to perform rectification of aerial images and (2) methane ebullition seeps on Goldstream Lake in the fall and spring of 2011 and 2012 using a survey-grade LEICA VIVA™ real-time kinematic Differential Global Positioning System (DGPS) with centimeter accuracy.

3.2.1　Fall 2011 and 2012 field surveys

We surveyed the lake perimeter and measured several permanently installed reference markers. We conducted detailed ebullition ice-bubble surveys in October 2011 2 weeks after image acquisition when lake ice was safe to walk on. The surveys were performed within two large polygons that are identified in Fig. 1f: one about 7 m from the eastern thermokarst shore and a second near the center of the lake. The surveyed polygons in the east and center of the lake covered ∼ 428 and ∼ 236 m^2, respectively, and were reported in detail in Walter Anthony and Anthony (2013) and Greene et al. (2014).

In October 2012, we performed bubble surveys 6 days after image acquisition in three other polygons (total area ∼ 200 m^2) randomly distributed across the lake (Fig. 1f). We performed bubble surveys earlier after image acquisition than in 2011 to avoid white ice condition. We used the seep identification method described by Walter Anthony et al. (2010).

3.2.2 Spring 2011 and 2012 field surveys

While field-based estimations of A-, B-, and C-type seeps were limited to survey plots covering about 13 % of the lake area, the locations of hotspot seeps were mapped across the whole lake using detailed DGPS surveys of open holes in October and April 2011 and 2012. Hotspots were detected visually at these times of the year as open water holes in lake ice.

3.2.3 Spring 2013 field surveys

In April 2013, we extracted several blocks of the full lake ice column at seep locations to investigate the temporal ebullition patterns that developed throughout the winter season.

3.3 Mapping ebullition seeps on lake ice

3.3.1 Pre-processing of images

We conducted the following image pre-processing. (1) We performed mosaicking of multiple images of Goldstream Lake to construct a complete image of the lake. This was achieved by using Agisoft PhotoScan Professional Software™ Version 0.9.0. (2) We then performed geometric image rectification with 22 DGPS-collected GCPs using a second-order polynomial transformation with bilinear resampling. The GCPs were distributed mostly around the lake perimeter. Some of them were identifiable reference points on the lake such as cattail vegetation and a LiCor methane analyzer installed on a platform on the lake. (3) For image enhancement we applied a feature linear transformation on all three visible spectral bands of the lake images using unstandardized principal component analysis (PCA). Both geometric and spectral image transformations were performed in ENVI™ image processing software, Version 4.8. PCA spectral transformation produced three independent principal component (PC) bands. The first band (PC 1 band) consisted of the variables that explained the most variance (> 98 %) in the data set attributing to bubble patches (Fig. 2, Supplement Sect. S1).

3.3.2 Identification of bubble patches on snow-free lake ice

We applied a classification technique based on object-based image analysis (OBIA) to semi-automatically identify and map methane ebullition bubble patches in the PCA-transformed images using eCognition Developer™ 8 (Lindgren et al., 2015). Our object-based classification method comprised two steps: (1) image segmentation, i.e., aggregation of homogenous image pixels based on their spatial and spectral homogeneity into meaningful clusters known as image objects, and (2) classification of image objects (Navulur, 2007; Blaschke and Strobl, 2001). Varying ice conditions on the lake such as (a) clear, dark congelation ice, (b) milky

white snow–ice, and (c) ice with shadows from neighboring trees added challenges to identifying ebullition bubble patches. We were able to resolve these challenges by integrating semantic information associated with image objects in classification (Lindgren et al., 2015). For this, the scene is first decomposed into meaningful regions that represent different areas of lakes such as vegetation and shadow, dark, and white ice. These regions are then organized in a conceptual image object hierarchy, creating a semantic network between different sized image objects – large-scale objects in the upper level called "super-objects", and small-scale objects in the lower level called "sub-objects" (Supplement Fig. S1; Lindgren et al., 2015). For example, the lake area is a super-object composed of sub-objects associated with various lake ice characteristics (e.g., shadow, dark black ice), whereas areas of specific lake ice characteristics are super-objects of our final target feature, ebullition bubble patches. At each level, image segmentation and classification are performed to delineate and label target regions. For example in the first level, segmentation is performed on the whole lake image to identify lake shore and lake. In the second level, only the lake region is segmented and image objects derived from the lake are classified into different lake ice characteristics. The process continued as it proceeded towards lower and finer classification levels until bubble patches were identified in the lake ice in the final stage. This approach of detecting image objects from coarser to finer scale has been described as an effective way to classify images in OBIA (Blaschke et al., 2008).

More information on this hierarchical approach of bubble-patch identification can be found in the Supplement (Supplement Sect. S2) and in Lindgren et al. (2015).

3.3.3 Identification of open-hole hotspots on snow-covered lake ice

In images acquired after the first snow fall, hotspots appeared dark against the snow-covered lake. Hence, they were mapped using a simple contrast and split segmentation technique in eCognition Developer™ (Definiens, 2007). This approach involves choosing a threshold value on the RGB image bands for the algorithm to maximize the contrast between hotspots and snow-covered lake pixels that separates the image content into dark objects (consisting of pixels below the threshold, i.e., hotspots) and bright objects (consisting of pixels above the threshold, i.e., snow-covered lake ice).

3.4 Statistical analysis

3.4.1 Interpretation of image data results

We extracted PC 1 gray values of individual ebullition bubble patches mapped in images from the year 2011 and 2012. PC 1 values of the image ranged between 0 and 255. Bubble patches are visually bright in true-color composite (RGB
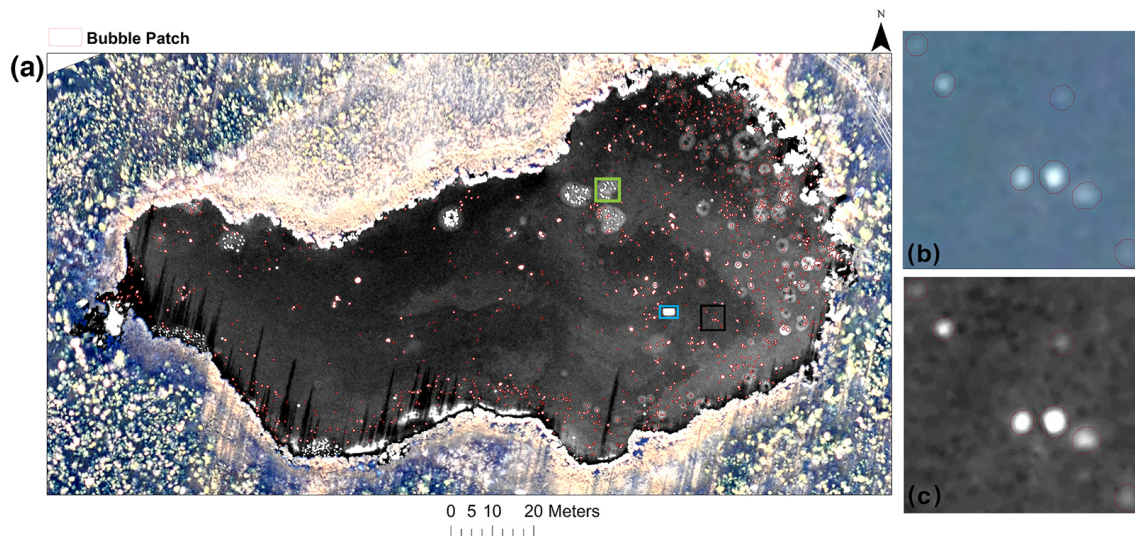
Figure 2. Panel **(a)** shows the 2011 bubble-patch map of Goldstream Lake overlaid on a principal component 1 image (PC 1, inverted). The land around the lake is shown in a true-color composite of red, green, and blue bands (RGB). Panels **(b)** and **(c)** show the area highlighted in the black box in panel **(a)** overlaid on RGB composite and PC 1 respectively. Bright bubble patches appear distinct against dark lake ice on PC 1. A rectangular wooden instrument platform in shown in the center of the lake (blue box) as well as clusters of lily pads (one example is highlighted by the green box) on the northern and southwestern parts of the lake (see Fig. 1) also appear bright on PC 1.

composite) images but appeared darker (i.e., low PC 1 values) than the surrounding lake ice in the PC 1 band (Supplement Fig. S2). Therefore, we inverted PC 1 values of bubble patches to make it visually intuitive, i.e., bubbles that appeared bright in natural color composite also appeared bright in the PC 1 band (Fig. 2). Henceforth, we refer to this brightness obtained in the inverted PC 1 as "PC 1 brightness".

We assessed the relationship of ebullition bubble-patch PC 1 brightness values with four distinct types of ebullition seeps that we identified during our field surveys. We performed an analysis of variance (ANOVA) to test the null hypothesis that the mean PC 1 values (and thus true bubble brightnesses via its inverse relationship with the PC 1) of four types of seeps are not significantly different. We applied a post-hoc Tukey's honest significant difference (HSD) test, in case the null hypothesis was rejected, to identify significantly distinct seeps. Results of this analysis are shown in Sect. 4.1.

3.4.2 Classification of bubble patches

We applied a supervised classification using a maximum-likelihood classifier (MLC) on the three original visible bands and the extracted PC 1 band to classify mapped bubble patches into four distinct seep classes. The MLC calculates a Bayesian probability function from the input training classes and then assigns each pixel in the image to the class of highest membership probability (Mather, 2009). We collected 98 random samples, 35 for training and 63 for validation, on the 2011 image and similarly 181 random samples, 50 for training and 131 for validation, on the 2012 image. The samples

were located at seep locations identified using field-collected DGPS data points.

The MLC approach categorized bubble patches solely based on the pixel spectral characteristics, i.e., only using the brightness values of the training samples. Since the size of bubble patches is also an additional important indicator of seep class and methane flux (Walter Anthony et al., 2010), in a subsequent step, we further refined our classification results by integrating size as an additional feature to more accurately assign bubble patches with a seep type (Supplement Sect. S3, Table S1). Finally, we estimated the seep density and mean whole-lake ebullition rate by assigning the mean long-term flux values for seep types provided by Walter Anthony and Anthony (2013) to our classified bubble patches.

3.4.3 Analysis of spatial distribution of bubble patches

We studied the spatial distribution of ebullition bubble patches as a function of distance from the eroding eastern thermokarst shore. For this, we divided the lake area into multiple 5 m wide zones starting from the eastern eroding margin as mapped in a 1949 aerial image (Fig. 1). Lake zones were created on both sides of the 1949 lake margin to cover the present-day lake area. We calculated the percent of lake ice area covered with ebullition bubble patches for each zone and then analyzed its relationship to the distance from the eastern shore lines of the lake observed in 1949, 1978, and 2012.

3.4.4 Analysis of temporal pattern of bubble patches

We evaluated the multi-temporal (year 2011 and 2012) variability of ebullition bubble patches and assessed their regularities in space and time. We utilized a marked point-process model to analyze spatial seep patterns in our multi-year bubble-patch data set derived from the images. Point-process modeling was performed on a set of bubble-patch centroids with their respective location and year information, which served as a marked point data set for the model, to derive and test the spatial characteristics of bubble-patch distribution against a null hypothesis based on complete spatial randomness. The null hypothesis suggests that the bubble patches are the results of a spatially random process over the study area and thus the difference of spatial patterns between years is random, i.e., the locations of bubble patches are independent when comparing between years (Bivand et al., 2008). For this, we generated a multi-type nearest-neighbor distance function derived from the locations of the bubbles mapped in the images using Gcross from the spatstat statistical package in R (Baddeley and Turner, 2005). Gcross first determines clustering parameters for the data set in the first year. These clustering parameters are then used to model the expected number of the second-year point given a certain distance from the first-year points if the second-year point placement is random relative to the first-year point placement. Based on the deviation between observed empirical value and expected theoretical value estimated by the model, we determined the stability of seep locations between 2011 and 2012. Similarly, we performed the multi-type nearest-neighbor distance function analysis using Gcross on the field data set of hotspot locations collected in year 2011 and 2012 to check regularity of hotspots.

We also considered that the centroid of a bubble patch, representing an ebullition bubble-patch point location, could move from one year to another due to changes in the shape and size of a bubble patch or changes in bubble-tube configuration in the sediment. We compared the overlap area between ebullition patches mapped in 2011 and 2012 images. If some area of a 2011 bubble patch appeared within the area of a 2012 bubble patch or vice versa, then we considered the bubble patch to be stable in location (i.e., reappearing). We assumed that the overlapping bubble patches originated from the same point-source seep. We checked location stability among four classes of overlapping patches that were defined by setting thresholds on area overlap: "all overlapping bubble patches", "more than 25 % area overlap", "more than 50 % area overlap", and "more than 75 % area overlap".

We used a map of open-hole hotspot seeps derived from UAV images to compare the frequency of hotspots with hotspot occurrences observed during multiple years of field-work by Greene et al. (2014).
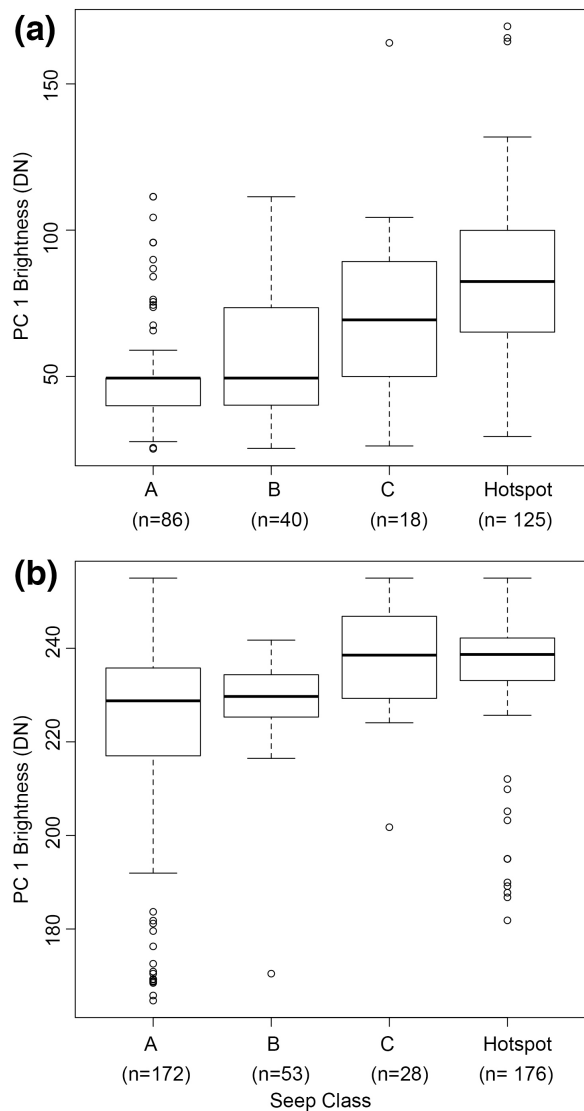
4 Results and discussion

4.1 Relationship between bubble-patch brightness and field-measured methane flux

We found that PC 1 brightness values of bubble patches correlated with the strength of field-measured methane flux of ebullition seeps (A, B, C and hotspot seeps). The lowest mean PC 1 brightness belonged to A-type seeps followed by B-type seeps in both 2011 and 2012 (Fig. 3). The highest mean PC 1 brightness was demonstrated by hotspots in 2011 but C-type seeps had slightly higher mean brightness in 2012 (Fig. 3). Our ANOVA test rejected the null hypothesis that the mean PC 1 values of the different seep types are the same suggesting significant distinctions between mean PC 1 brightness values of different seep classes. Further post-hoc analysis using Tukey's HSD test demonstrated that C- and A-type, hotspot and A-type, and hotspot and B-type seeps are significantly distinct based on their mean PC 1 with p values < 0.05 (Supplement Table S2). We thus conclude that higher-flux seeps (hotspot and C-type) are associated with brighter bubble patches, and lower-flux seeps (A- and B-type) are associated with darker bubble patches.

An absolute discrimination of individual seep type based on brightness was not supported by the post-hoc tests due to overlapping brightness ranges between different seep types (Fig. 3). This is likely because ebullition is episodic with varying bubbling rates over time and because individual low-flux methane seeps were not resolved given the spatial resolution of the image. A possible explanation for low PC 1 brightness of some hotspots is that fresh thin nighttime ice temporarily covered some hotspots on the image acquisition day, allowing the formation of few small white gas bubbles, while much of the remaining gas escaped through cracks in the thin ice, resulting in low true brightness for these high-flux seeps. We have observed this phenomenon on several occasions during our field visits in early winter and spring, particularly on days when temperatures stayed low and hotspots were covered with a few millimeters of ice with small bubbles beneath (Fig. 4); these hotspots usually open up when atmospheric temperature rises again during the day. Conversely, hotspots that remained open could not be identified in our snow-free lake ice imagery due to spectral similarities between open water and clear black ice (Fig. 1). ANOVA analysis was only performed on ice-covered hotspots.

We found that a large number of A-type seeps clustered together were not mapped as individual bubble patches but rather as a single large bubble patch. A-type seeps and high-flux seeps that were close together were also mapped in a single feature associated with a brighter bubble patch. Therefore, some A-type seeps showed high PC 1 brightness values. Similar to A-type seeps, occasionally individual B-type seeps were also not distinct. In a time series analysis of bubbling frequency by A- and B-type seeps, Walter Anthony et al. (2010) showed that bubbling from these shallow-sourced

Figure 3. Box plots are shown of PC 1 brightness values for bubble patches with different classes of seeps in 2011 **(a)** and 2012 **(b)**. Significant differences (p values < 0.05) based on their PC 1 mean brightness values were found between C- and A-type seeps, hotspot and A-type seeps, and hotspot and B-type seeps for 2011; and C- and A-type seeps, hotspot and A-type seeps for 2012. SD signifies standard deviation.

| | PC 1 Brightness | | | |
| | Year 2011 | | Year 2012 | |
Seep Class	Mean	SD	Mean	SD
A-type	51.86	18.92	222.34	20.83
B-type	58.29	23.83	228.76	10.04
C-type	72.14	32.51	237.71	11.58
Hotspot	84.59	28.03	235.86	12.57

seeps is highly seasonal. Bubbling rates are high in summer when surface sediments are warmer, and low in winter when sediments cool down. Bubble traps left in place over these seep types year round revealed that low-flux seeps can have periods of no bubbling for up to several months. Ice blocks harvested by us in spring over seeps marked as A-type seeps in October confirm this pattern (Supplement Fig. S3). It is very likely that A- and B-type seep conduits were present in the sediments, but not actively bubbling during the 2- and 4-day periods after ice formation captured by the 2011 and 2012 imagery. Thus they did not appear under the given spatial resolution of the image and its specific acquisition time. Also, bubble traps placed over C-type seeps year round revealed that these seeps can also undergo long periods (weeks to months) of no bubbling, but when they bubble, the bubbling rates are usually very high (Walter Anthony et al., 2010). This intermittent flux behavior probably contributed to some discrepancies in the relationship between bubble-patch brightness derived from images that captured a snapshot of ebullition activity and methane flux values of seeps estimated from long-term field observations (Table 1).

In other parts of Goldstream Lake, especially along the eastern shore, we found large patches of many individual ebullition bubbles (each typically 3 to 10 mm diameter) that formed large diffuse patches rather than clustering as tightly packed bubbles the way A, B, C, and hotspot seeps do. In our optical images, these ebullition bubbles appeared as irregular patches of fuzzy, white-colored bright ice with some bright regular bubble spots (Fig. 4). Therefore, the brightness values corresponding to the surrounding diffuse patches were assigned to other seeps, particularly to low-flux seeps that were within the patch and had not expressed completely when the images were acquired. Until recently, these millimeter-scale ebullition bubbles were only recorded in transect-survey data as "tiny-type" seep but never assigned a mean daily flux value or included in whole-lake ebullition estimates due to a lack of associated flux field measurements. Recent flux measurements made continuously year round with submerged bubble traps on the tiny-type seep class in Goldstream Lake and other lakes suggest that fluxes from these seeps may also be important (Walter Anthony et al., unpublished). Analysis of bubbles collected with bubble traps placed over tiny-type seeps revealed that these bubbles were 60–80 % methane in volume (Walter Anthony et al., unpublished). When we extracted an ice block in spring 2013, we observed that tiny-type ebullition had been frequent throughout winter, resulting in long, vertically oriented stacks of tiny ebullition bubbles trapped in ice (Fig. 4).

4.2 Classification of bubble patches

The overall MLC classification accuracy for differentiating seep types was ~ 50 % for both 2011 and 2012 (Supplement Table S3). The classifier performed better to identify the lowest flux seeps (A-type) and the highest flux seeps
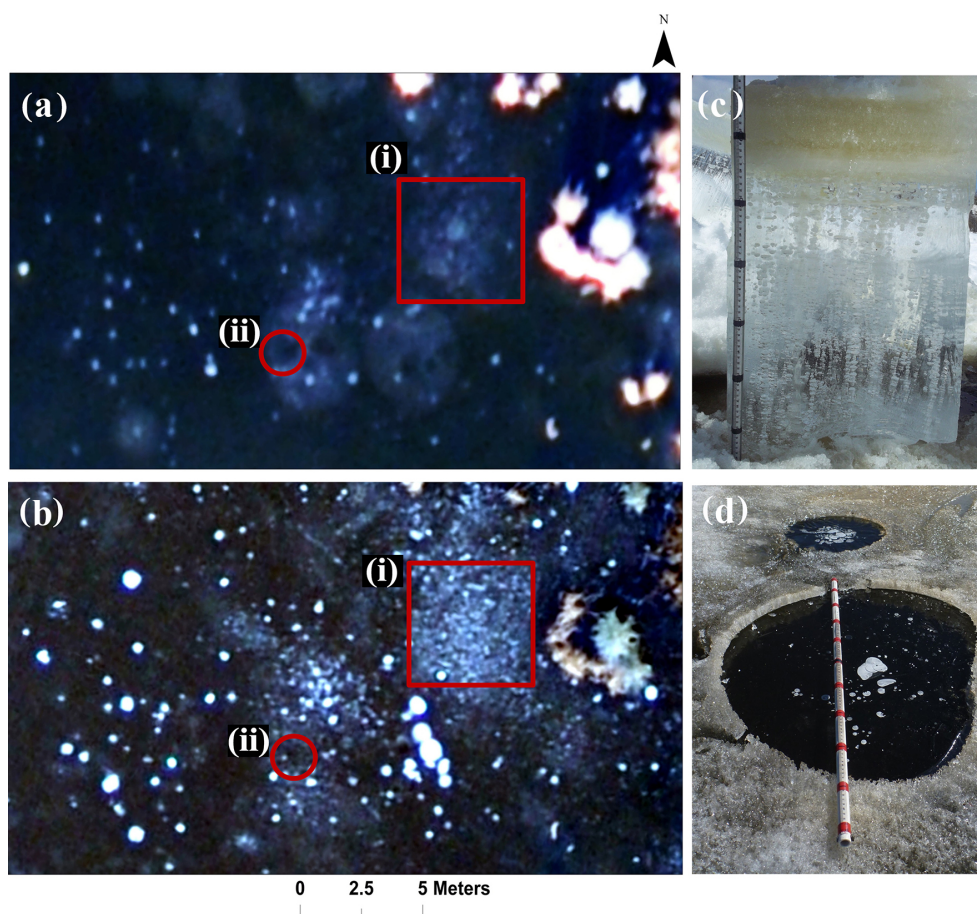
Figure 4. Panels **(a–b)** show a close-up of low-altitude aerial images from Goldstream Lake (~ 10–15 m from the eastern thermokarst margin), Fairbanks, Alaska (the same aerial extent shown in **(a)** October 2011; **(b)** October 2012). The red box (i) highlights a densely packed cluster of millimeter-scale ebullition bubbles (tiny-type seep) in both years. A few B- or C-type seeps also occurred among the tiny-type ebullition bubbles inside the area marked by the red square. The red circle (ii) shows an area of hotspots. In 2011, the hotspots appear dark, similar to clear black ice surrounded by a bright circular patch, likely hoar frost formed around open water holes. **(c)** An ice block cross section with the tiny-type seep bubbles in the bubble cluster area is shown in area (i). **(d)** In April 2012, the hotspot highlighted in area (ii) seems to be mostly covered with a very thin layer of fresh black ice with a few bubbles trapped beneath; however, there was a mostly ice-free cavity in the ice above the locations of the hotspots while the rest of the lake ice was still ~ 50 cm thick.

Table 1. Seep density and estimated mean whole-lake ebullition flux of Goldstream Lake, Fairbanks, Alaska, was derived from 2011 and 2012 optical aerial image data set and from ground surveys. The ground survey estimates are from previously published studies by Walter Anthony and Anthony (2013) and Greene et al. (2014) based on ground surveys conducted over multiple years (2007–2011) at Goldstream Lake.

| | Seep density (seeps m^{-2}) | | | | | Mean whole-lake ebullition |
Surveys	A	B	C	Hotspot	All seeps	(mL gas m^{-2} d^{-1})
Aerial (14 Oct 2011)	0.026	0.059	0.019	0.017	0.119	174 ± 28
Aerial (13 Oct 2012)	0.061	0.083	0.021	0.021	0.185	216 ± 33
Ground surveys	0.366	0.099	0.032	0.011	0.508	170 ± 54

(hotspot-type). B-type and C-type seeps showed high error of commission, mostly arising from the misidentification of A-type seeps and hotspots. C-type seeps had the largest error of omission since they were mostly misclassified as B-type seeps in 2011 and hotspots in 2012.

Generally higher densities of A-type seeps (and also slightly in B- and C-type seeps) in ground surveys (Walter

Anthony and Anthony, 2013; Greene et al., 2014) compared to aerial images (Table 1) can be explained by the time in which observations were made and image resolution. Results reported in Walter Anthony and Anthony (2013) and Greene et al. (2014) are based on ground surveys conducted over multiple years (2007–2011) at Goldstream Lake usually 1 to 2 weeks following freeze-up when ice was safe to walk on (Walter Anthony et al., 2010). Since our aerial surveys were conducted only 2–4 days after ice formation, and the frequency of bubbling events from A-type seeps is often weeks to months in winter, it is not surprising that the field surveys several weeks after ice formation capture an order of magnitude more A-type seep bubbles. Additionally, it is very likely that some active A-type seeps that occurred in very small patches were not distinct under the given resolution of the aerial images. Relatively more frequent bubbling in B- and C-type seeps allows for similar seep density values between ground surveys and aerial images; however, as expected, the 2012 seep densities are closer to the ground-ice survey values due to (a) more time since freeze-up and (b) a much higher barometric pressure drop preceding the aerial image acquisition in October 2012 compared to October 2011. It is well established that ebullition dynamics are related to changes in barometric pressure (Mattson and Likens, 1990; Fechner-Levy and Hemond, 1996; Scandella et al., 2011).

The comparison of hotspot densities in optical images vs. ground surveys in Table 1 also shows the expected pattern. The ground-survey data of hotspots reflect multiple years of surveys of whole-lake hotspots when ice is thick enough to safely walk on. When ice is very thin a few days after freeze-up, more open holes are present on the lake and classified as hotspot seeps in aerial images. A week or more later, many holes freeze over and will be classified as C-type seeps in ground surveys. This could have also led to a high classification error for C-type seeps. The total density of C-type and hotspot seeps combined remains consistent (~ 0.04 seeps m^{-2}) in both aerial and ground observations (Table 1). This also indicates that some of the seeps identified as hotspots several days after freeze-up in aerial photos really become what we classify as C-type seeps (ice-sealed at the surface) within a week or more following freeze-up.

4.3 Estimation of whole-lake methane flux

Our image-based analysis shows the whole-lake flux to be 174 ± 28 and 216 ± 33 mL gas m^{-2} d^{-1} for the year 2011 and 2012, respectively. The uncertainty terms are based on the standard error of the means of field-measured fluxes for seep classes. The higher-flux estimate in 2012 is due to the presence of a large number of bubble patches in 2012 (0.185 seeps m^{-2}) compared to 2011 (0.119 seeps m^{-2}) (Table 1). The field-based estimate of whole-lake ebullition for Goldstream Lake using ice-bubble transect surveys (170 ± 54 mL gas m^{-2} d^{-1}), was slightly at the low end of

the estimates based on optical imagery analysis from 2011 and 2012 respectively. It is conceivable that the field-based transect surveys might yield a lower flux than whole-lake seep analyses given that seeps are spatially rare, and field surveys often cover < 1 % of the lake surface area (Walter Anthony and Anthony, 2013). However, on Goldstream Lake, where our field transect bubble surveys covered 13 % of the lake area for A, B, and C-type seeps and 100 % of the lake area for hotspots, the higher estimates based on optical imagery appear to be due to an overestimation of hotspots in the early-acquisition date aerial image analysis. It is important to note that while the whole-lake methane flux estimates from our aerial survey are close to those based on ground surveys, the flux estimates for individual seep types may vary between the methods. It is also possible that with aerial surveys we are underestimating the total contribution of methane flux from low-flux seeps because they had not expressed completely when we acquired our aerial photos and that we are overestimating the contribution from high-flux seeps.

4.4 Spatial distribution of bubble patches in relation to the thermokarst lake margin

High methane production in response to thermokarst activity on the Goldstream Lake is evident from the distribution pattern of ebullition bubble patches at the eroding margins in different years. We found a strong inverse relationship (R^2 values of 0.86 and 0.79 for the years 2011 and 2012, respectively, with p values < 0.05) between the ebullition bubble patch area covering the lake ice and the distance from the rapidly eroding eastern margin of the lake (Fig. 5). The percent surface area of lake ice covered with ebullition bubble patches ice decreased with distance from the active erosion margin. Thermo-erosion as well as talik growth on the expanding eastern shore releases labile Pleistocene-aged organic matter as permafrost thaws, enhancing anaerobic microbial activity in the lake and talik sediments, and leading to enhanced methane emissions along this shore (Brosius et al., 2012; Walter Anthony and Anthony, 2013). Holocene-aged carbon from vegetation and active layer soils is also eroded and additionally produced within the lake, further fueling microbial methane production (Walter Anthony et al., 2014). Walter Anthony and Anthony (2013) found an interesting relationship between lake bed morphology and ebullition bubble seep density on Goldstream Lake. They found dense clusters of ebullition seeps distributed ~ 10 m apart across the lake that matched the spacing of baydjarkah on the lake bed. This indicates that most of the methane gas bubbles originated from the top of baydjarakhs, consisting of organic-rich thawed permafrost soil. While we did not conduct specific analyses in our study, such patterns should be detectable in optical remote sensing images of lake ice as well.

We observed fewer ebullition bubble patches in the center of the lake, which we interpret as a sign that labile Pleistocene-aged organic carbon in the talik under this area
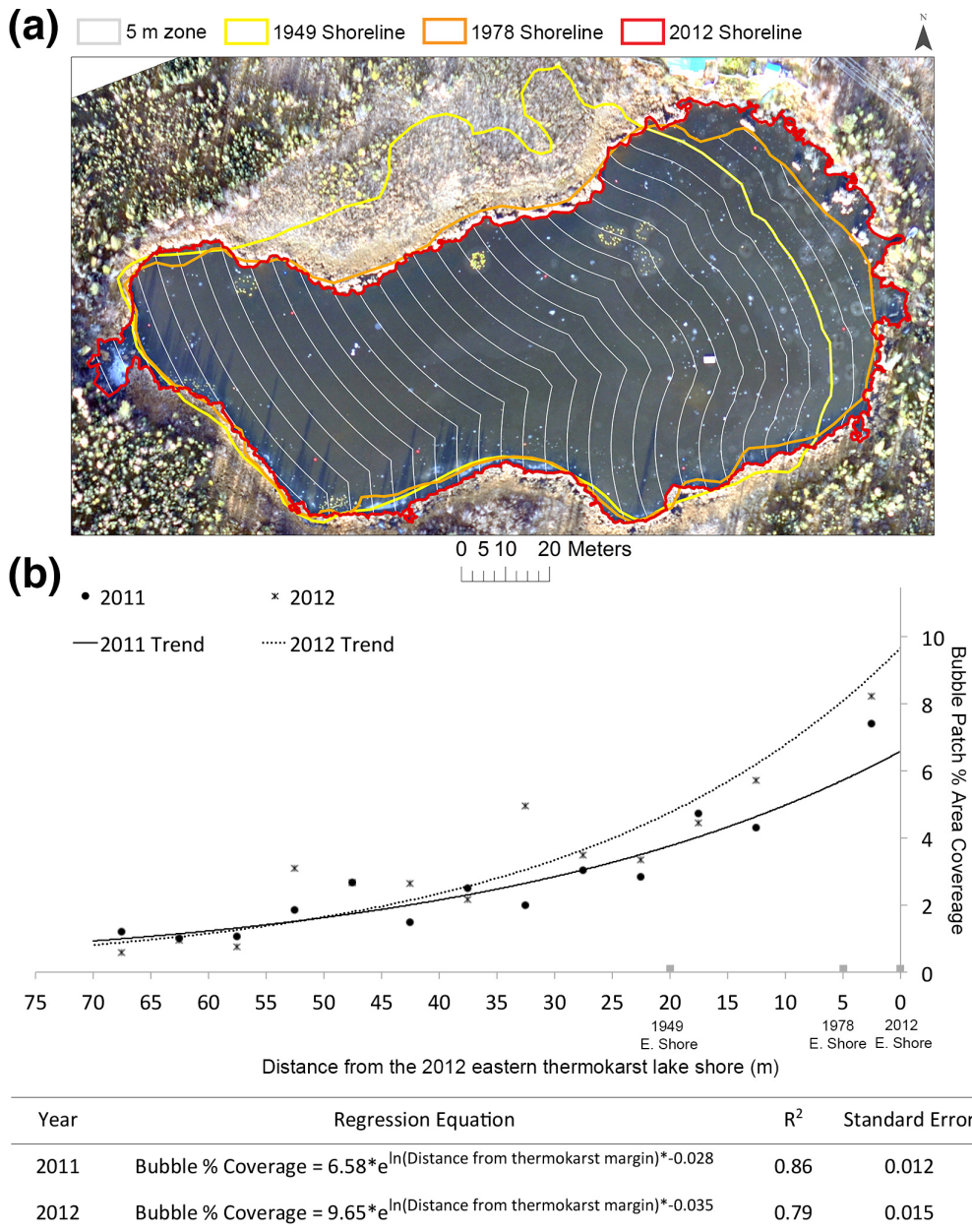
Figure 5. Panel **(a)** shows an aerial image acquired on 14 October 2011 with lake perimeters from 1949 (yellow shoreline), 1978 (orange), and 2012 (red). Lake area change between 2011 and 2012 is minimal. The lake is divided in zones of 5 m width (white lines), for which the percent of bubble patch area was calculated for comparison to the distance from the rapidly expanding eastern lake margin. Panel **(b)** shows the inverse exponential relationship between bubble patch percent cover and distance from the eastern thermokarst margin of Goldstream Lake, Fairbanks, Alaska.

has been largely depleted, and unlike at the edge along the active erosion margin, there is no significant additional accumulation of ancient labile carbon in the lake center (Brosius et al., 2012). Radiocarbon dating of bubble patches found in the lake center showed that these seeps originate from Holocene-aged and more recent organic matter that is found in the upper lake sediments (Brosius et al., 2012). Generally, methane bubbling was the lowest along the 1949 eastern lake margin and the highest along the 2012 eastern lake margin (Fig. 5), indicating that depletion of labile carbon progressed since these areas were included in the lake, and the active thermo-erosion margin migrated eastward. This shows that optical remote sensing is a powerful tool to understand the spatial variability of methane ebullition on thermokarst lakes.
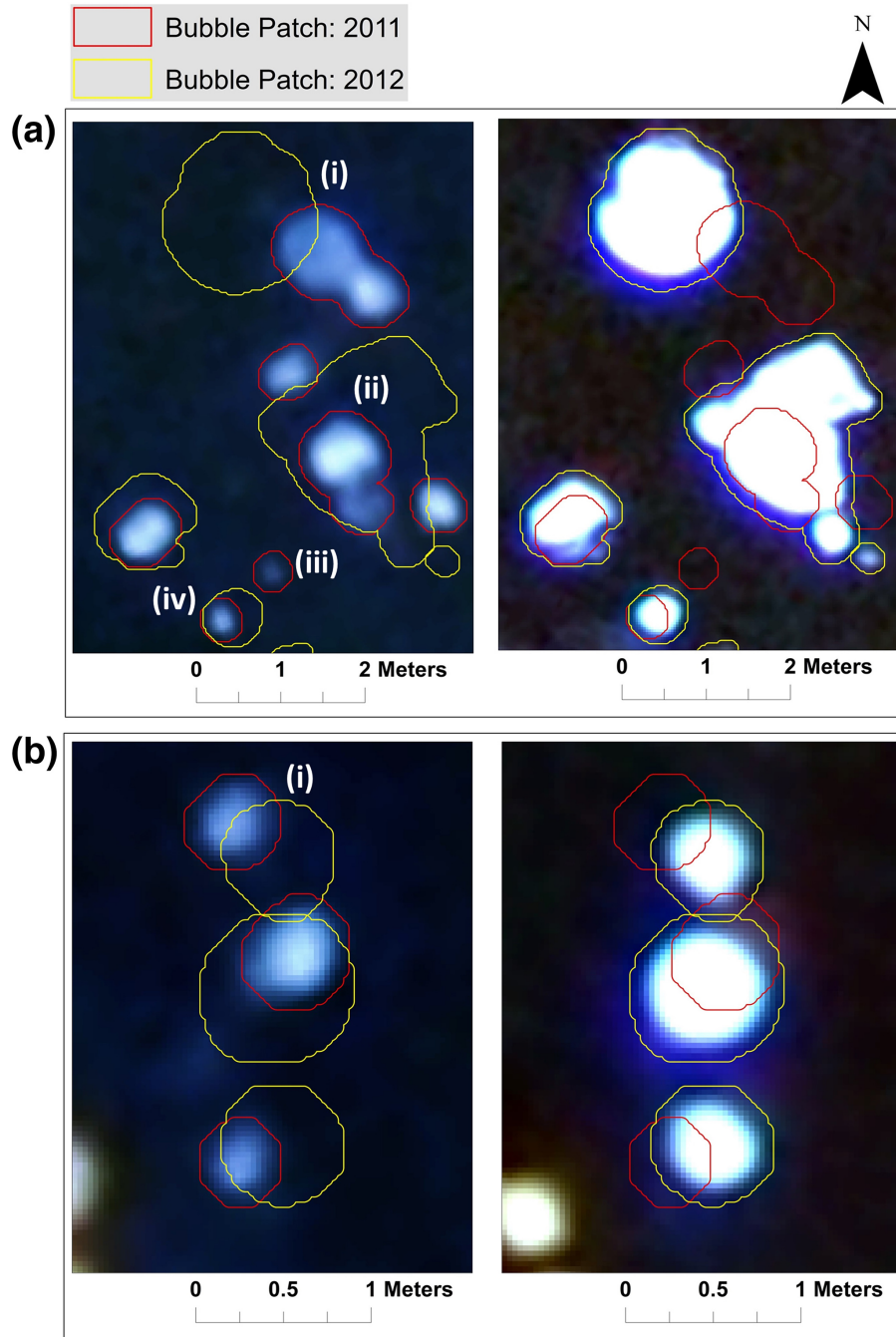
Figure 6. A comparison of bubble patches visible in thin lake ice 2 days after freeze-up in October 2011 (left-side images) and 4 days after freeze-up in October 2012 (right side images) is shown. Image pairs in **(a)** and **(b)** represent the same locations in 2011 and 2012. Four major characteristics of bubble patches are identified in panel **(a)**: (i) bubble patches may shift up to 50 cm in location (geolocation error < 20 cm) in non-consistent directions; (ii) bubble patch size and morphology varies between years during the first few days following freeze-up; (iii) bubble patches visible during the first few days of freeze-up in one year are not visible during the first few days of freeze-up in another year; and (iv) bubble patches are similar in shape but not in size. Panel **(b)** shows another example of horizontal shift of bubble patches (i).

4.5 Multi-year comparison of bubble patch characteristics: 2011 and 2012

We observed four possible characteristics of bubble patch dynamics in our images (Fig. 6). (i) Bubble patches may move horizontally; (ii) bubble patches do not maintain the same morphology between years (e.g., single bubble patches reappear in a cluster of multiple patches the next year or vice-versa); (iii) bubble patches appear in an image in one year and not another; and (iv) bubble patches maintain the location and shape but patch size is different between the years. It is important to note that these observations are made during the two very short windows of time 2–4 days after freeze-up. Our analysis does not take into account the changes in long-term bubble patch morphology. Hence, it is important to highlight that the characteristics of bubble patches are driven by the dynamics of bubble formation and transport, hydrostatic pressure, and ice growth. Other changes in the characteristics of bubble patches could be because of evolution of point sources or changes in point-source conduits (bubble tubes) in the sediment (Walter et al., 2008; Scandella et al., 2011). Atmospheric pressure dynamics can also strongly impact bubbling over short timescales, resulting in different ice-bubble patterns one year from the next if insufficient time passes to allow all seeps to be expressed in the lake ice cover. Field measurements have shown that ebullition is inversely related to changes in hydrostatic pressure (Mattson and Likens, 1990; Varadharajan, 2009; Casper et al., 2000; Glaser et al., 2004; Tokida et al., 2005; Scandella et al., 2011). A significant air pressure drop during the week preceding image acquisition in October 2012 may have allowed methane that previously accumulated in the sediment during high-pressure days to rise up into the water column, manifesting itself as larger numbers of bubbles (Fig. 7), and larger and brighter bubble patches in the lake ice (Fig. 6). Conversely, air pressure change in October 2011 was not large enough to enhance ebullition before the image was acquired. As a result, bubble patch density was 55 % higher in 2012 ($0.185\,\mathrm{m}^{-2}$) 2012 compared to 2011 ($0.119\,\mathrm{m}^{-2}$). Similarly, the estimated mean whole-lake ebullition was 24 % higher in 2012 compared to 2011 due to different atmospheric pressure dynamics. However, the general spatial distribution of bubble patches remained the same between the two years: ebullition bubble patches were more concentrated towards the eastern thermokarst lake shore.

We rejected the null hypothesis of complete spatial randomness to show that the difference in spatial patterns of bubble patches and hotspots between years is not random, i.e., that the locations of seeps in the years 2011 and 2012 are not independent. The Gcross distribution function showed that a statistically significant number of second-year bubble-patch center points are less than 2 m away from the first-year center points and that there are far fewer than expected that are 3 m or more apart (Fig. 8a). For the hotspots, a statistically significant number of seeps moved less than a me-

ter (Fig. 8b). Since our image rectification accounted for a geolocation error of less than 20 cm and DGPS geolocation error is even smaller and considered negligible, we conclude that the seep locations are consistent between years 2011 and 2012.

Based on our DGPS data, the number of hotspots was relatively stable among the various surveys with about 105 hotspots for the whole lake as the average of various measurements during different years and spring and fall field seasons (Greene et al., 2014). UAV-based aerial images taken 5 days after ice formation when snow covered the lake also demonstrated close agreement with the hotspot seep numbers and locations. We were able to identify 78 dark open water holes in the white, snow-covered UAV lake image acquired in early winter of 2012. Among these 78 locations there was a total of about 95–100 active open-hole hotspot seeps since some large, irregularly shaped holes consisted of multiple, coalesced holes produced by hotspot seeps of close proximity (Supplement Fig. S4).

When we compared the location of bubble patches in 2011 and 2012, we found that 47.2 % of a total of 1195 ebullition bubble patches mapped in 2011 reappeared in 2012, which is 35.7 % of a total of 1860 ebullition bubble patches mapped in 2012. We found that 37.5, 30, and 17.7 % of bubble patches mapped in 2011 reappeared in 2012 with an overlap area of "more than 25 %", "more than 50 %", and "more than 75 % area", respectively. We expect that if more time passed between the time of freeze-up and aerial image acquisition date we would see an even higher percentage of seep location re-occurrences because more seeps would be actively expressed.

We also observed a relationship between bubble-patch brightness and location stability of bubble patches. Very bright patches in 2012 seemed to appear at locations where bubble patches were already observed in 2011. This could indicate locations of high-flux seeps where methane was able to rise through the sediment even under relatively high hydrostatic pressure conditions that we observed in October 2011. Based on our bubble patch classification results (Table 1), we also noticed that seep density of high-flux C- and hotspot-type seeps is less variable during our study period compared to low-flux A- and B-type seeps. However, long-term remote sensing and ground-based observations are required to further test our hypothesis of seep regularity that high-flux seeps are temporally more stable in their location than low-flux seeps. Additionally, long-term data may also help to account for the difference in pressure and look at possible changes in seep type over the years.

The regularity of bubble patches observed despite the differences in atmospheric pressure conditions following the lake freeze-up events in 2011 and 2012 as well as the location stability of hotspots indicates that a large number of point-source seeps in thermokarst lakes are stable over at least annual timescales. Walter Anthony et al. (2010) also found seeps to maintain stable locations in Goldstream Lake
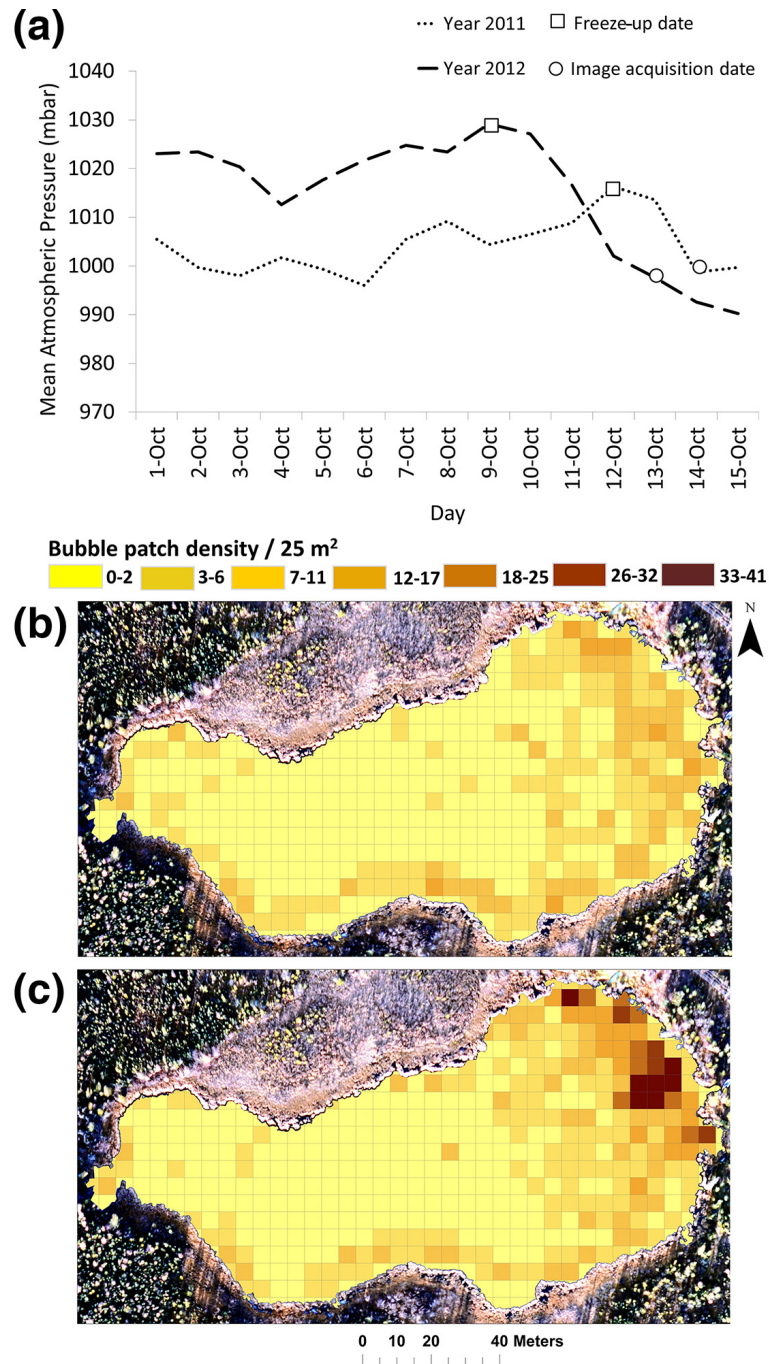
Figure 7. (a) The graph of mean daily atmospheric pressure (mbar) observed between 1 and 15 October in 2011 and 2012 shows that the magnitude of atmospheric pressure drop prior to image acquisition was twice as high in 2012 and 2011; pressure drops are known to induce ebullition. Bubble-patch density is shown in a 5×5 m grid as seen in the October images of the year **(b)** 2011 and **(c)** 2012. Generally darker grid cell colors in panels **(b)** and **(c)** suggest a higher density of seeps in 2012 compared to 2011, which is consistent with (1) a 2-times longer period of ice formation (4 days in 2012 vs. 2 days in 2011) for bubbles to accumulate and (2) atmospheric pressure patterns. The spatial distribution of bubble patches clearly shows a higher concentration of methane emission along the rapidly expanding eastern thermokarst margin in both years.
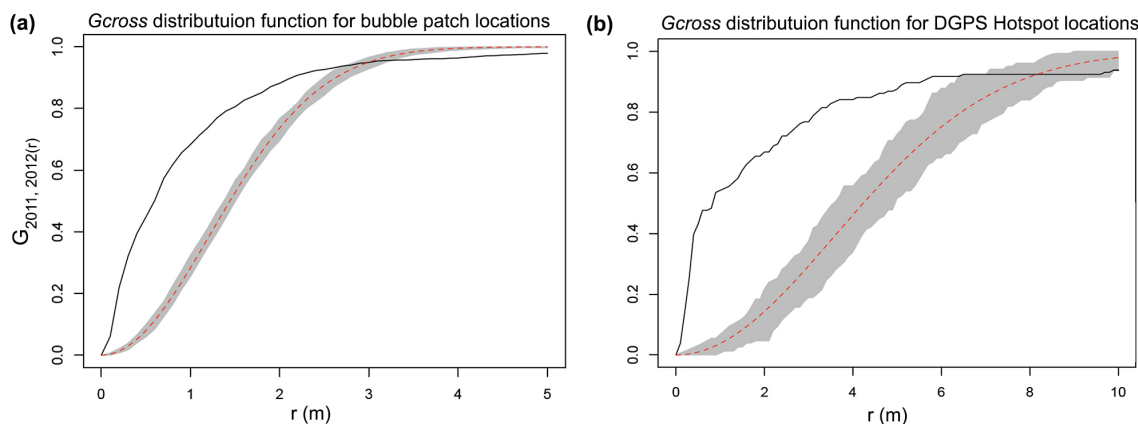
Figure 8. Cumulative distribution function of distances (r) is shown for between seeps identified in two different years 2011 and 2012. The black line shows actual observed data and the red line shows the theoretical expected value assuming the points are completely random. The gray shaded area shows a theoretical seep distance function for a random seep distribution (95 % confidence band). The deviation between the observed empirical value (black curve) and theoretical expected value (red curve) suggests that a large and statistically significant number of seeps show spatial dependence between 2011 and 2012. **(a)** Distance function for bubble patches derived from the image data set. The actual curve is well above the theoretical curve over separation distances of 0 to 2 m; and thus a statistically significant number of second-year bubble patch center points are less than 2 m away from the first-year center points. The actual curve is below the theoretical curve at the top after 3 m distance separation, suggesting that there are a far fewer number of seeps at large distances. **(b)** Distance function for seeps derived from DGPS field-measured hotspots. The observed function for the DGPS hotspot locations rises almost vertically over separation distances of 0 to 1 m deviating away from the theoretical function, i.e., a statistically significant number of hotspot seeps did not move much from the first-year location.

when submerged bubble traps were placed over individual seeps to monitor their ebullition dynamics for periods of up to 700 days. In Siberia one hotspot seep location was marked and found stable for at least 8 years (Walter Anthony et al., 2010).

5 Benefits and challenges of aerial image analysis for ebullition seep mapping

We found numerous significant benefits of using aerial images for characterizing ebullition seeps on lake ice. Aerial images of early winter lake ice without snow cover allowed us to map and characterize bubble patches on the entire lake surface as well as assess their spatial distribution more accurately. Snow-covered lake ice images allowed us to map open-hole hotspots. We were able to differentiate high-methane-emitting seeps from low-methane-emitting seeps on the lake based on PC 1 brightness values of bubble patches. Image-derived estimates of seep densities by class agreed with those of field-based survey methods, except for some overestimation of hotspots and underestimation of A-type seeps. We were able to differentiate lake areas with high seep densities versus low seep densities; having this ability is especially useful for quantifying methane ebullition on larger lakes that are harder to survey extensively by foot.

Our results also imply a potential to apply high-resolution optical images at a regional scale to quantify relative methane flux from many lakes, which at a minimum should allow

for the classification of high-ebullition versus low-ebullition lakes and their distribution in a region. It is important to note that while image analysis is useful to comprehensive mapping of lake ice bubbles, for the estimation of whole-lake methane emissions, this technique should be coupled with bubble-trap field measurements and laboratory measurements of methane concentration in bubbles.

But because ebullition is a temporally dynamic phenomenon, our ability to accurately identify the distinct seep type of bubble patches on a snapshot of ebullition activity during only 2 and 4 days since lake ice formation is limited. The morphology and distribution of bubbles can undergo significant changes in response to freeze/thaw cycles during winter (Jeffries et al., 2005). Furthermore, ebullition is highly controlled by the balance between atmospheric pressure and sediment strength, making it an episodic phenomenon (Varadharajan, 2009; Scandella et al., 2011). Ebullition is triggered following the fall of hydrostatic pressure or after a sufficient volume of gas is produced in the sediment that allows bubble tubes or gas conduits in lake sediments to open or dilate (Scandella et al., 2011). Bubbles previously trapped in lake sediment then break out through these open bubble tubes and rise up in the water column. Moreover, microbial activity of methane-producing bacteria is temperature-dependent. As a result, seep ebullition slows down when the lake surface sediments cool down in winter and it increases as lake sediment warms up in summer (Walter Anthony and Anthony, 2010). Therefore, discrepan-

cies arise in estimates of the number of seeps and seep morphology derived from observations made at different times of the ice cover season (Wik et al., 2011). Ideally, optical image acquisition would occur at least several weeks following freeze-up of lakes to allow more time for seep expression in lake ice. Unfortunately, snow-free conditions several weeks after freeze-up is rare in many regions of the Arctic; and early snow cover inhibits the mapping of bubble patches with optical data.

SAR data have an advantage over optical remote sensing data in detecting methane bubbles trapped in lake ice under snow cover conditions (Walter et al., 2008; Engram et al., 2012). Engram et al. (2012) showed that particularly L-band SAR data acquired in the fall have the potential to estimate whole-lake methane ebullition since a longer-wavelength L-band is able to detect bubbles under other conditions such as the presence of snow, a thin layer of white ice, and aquatic vegetation. However, the moderate spatial resolution of current L-band SAR systems can be a limiting factor to estimate methane emission from small lakes and to capture delicate spatial patterns of ebullition seeps on lakes. SAR lake images further tend to have false backscatter signals from the lake shore (Walter et al., 2008; Engram et al., 2012), therefore limiting its usability in proximity to shores (about 1 pixel around lake shores is excluded in SAR analyses) where we showed an important component of ebullition may take place on eroding thermokarst margins. Thus, high-resolution optical images can supplement SAR-based studies by revealing the location of methane ebullition seeps and their types on the lake more precisely. Our study shows that optical high-resolution remote sensing methods have the potential, given the caveats raised above, to improve understanding of spatial and temporal variability of ebullition and therefore the dynamics of microbial processing of organic matter within an individual lake.

6 Conclusions

It is important to understand the dynamics of methane ebullition from thermokarst lakes to estimate the amount of carbon release from thawing permafrost and to evaluate its feedback to the global carbon cycle. Our study focusing on Goldstream Lake, Interior Alaska, shows that high-resolution optical remote sensing is a promising tool to map the distribution of point-source methane ebullition seeps across an entire thermokarst lake surface, a task that is difficult to achieve through field-based surveys alone. This method helps to reveal the location and relative sizes of high- and low-flux seepage zones within lakes. We also demonstrated that a large proportion of ebullition seeps in the study lake were location-stable over at least two winter seasons in the 2011–2012 observation period. Such observations may be used to indirectly characterize permafrost carbon mobilization in a lake since lake portions with greater numbers of high-flux

seeps likely indicate either the presence of rapidly thawing organic-rich permafrost deposits or eroding lake margins. Our approach is also applicable to other regions and will help to characterize methane ebullition emissions from seasonally ice-covered lakes, including thermokarst and non-thermokarst lakes in tundra and boreal zones. It will help to differentiate lakes in a region based on methane emission by estimating ebullition seep density, and their relative methane flux. This differentiation could potentially be used to identify presence or absence of organic-rich permafrost deposits such as yedoma in the area. For example, yedoma-type thermokarst lakes, such as Goldstream Lake, where large amounts of labile carbon is readily available for microbes to decompose, emit more methane than non-yedoma-type thermokarst lakes. This can be a useful supplement to surveying soil carbon pools and yedoma distribution at a regional scale. Multi-temporal spatial information derived from remotely sensed optical data allows the identification of variables that control methane ebullition dynamics and spatial patterns. However, the timing of optical image acquisitions is a critical and a potentially limiting factor, with respect to both atmospheric pressure changes and snow/no-snow conditions during early lake freeze-up. Therefore, high-resolution remotely sensed optical images in combination with SAR and field data could be a very valuable tool to improve the estimation of methane emission from lakes at the regional scale.

Author contributions. G. Grosse and K. M. Walter Anthony conceived this study. P. R. Lindgren developed the method, performed data analysis, and wrote the manuscript with significant input from all co-authors. P. R. Lindgren, G. Grosse, and K. M. Walter Anthony were responsible for the field work.

References

Baddeley, A. and Turner, R.: Spatstat: An R package for analyzing spatial point patterns, J. Stat. Softw., 12, 1–42, www.jstatsoft.org (last access: August 2014), ISSN: 1548–7660, 2005.

Bastviken, D.: Methane emissions from lakes: Dependence of lake characteristics, two regional assessments, and a global estimate, Global Biogeochem. Cy., 18, 1–12, doi:10.1029/2004GB002238, 2004.

Bastviken, D., Tranvik, L. J., Downing, J. A., Crill, P. M., and Enrich-Prast, A.: Freshwater methane emissions offset the continental carbon sink, Science, 331, 6013, doi:10.1126/science.1196808, 2011.

Bivand, R. S., Pembesma, E. J., and Gomez-Rubio, V.: Applied Spatial Data Analysis with R, Springer, New York, 2008.

Blaschke, T. and Strobl, J.: What's wrong with pixels? Some recent developments interfacing remote sensing and GIS, GIS – Zeitschrift für Geoinformationssysteme, 14, 12–17, 2001.

Blaschke, T., Lang, S., and Hay, G. J.: Object based image analysis: Spatial concepts for knowledge-driven remote sensing applications, Springer-Verlag Berlin, Heidelberg, Germany, 2008.

Brosius, L. S., Walter Anthony, K. M., Grosse, G., Chanton, J. P., Farquharson, L. M., Overduin, P. P., and Meyer, H.: Using the deuterium isotope composition of permafrost meltwater to constrain thermokarst lake contributions to atmospheric CH$_4$ during the last deglaciation, J. Geophys. Res., 117, G01022, doi:10.1029/2011JG001810, 2012.

Casper, P., Maberly, S. C., Hall, G. H., and Finlay, B. J.: Fluxes of methane and carbon dioxide from a small productive lake to the atmosphere, Biogeochemistry, 49, 1–19, 2000.

Definiens: Segmentation Algorithms In Definiens Developer 7 Reference Book, Document Version 7.0.0.843, 15–27, Definiens AG, München, Germany, 2007.

Engram, M., Walter Anthony, K. M., Meyer, F. J., and Grosse, G.: Synthetic aperture radar (SAR) backscatter response from methane ebullition bubbles trapped by thermokarst lake ice, Can. J. Remote Sens., 38, 667–682, 2012.

Fechner-Levy, E. J. and Hemond, H. F.: Trapped methane volume and potential effects on methane ebullition in a northern peatland, Limnol. Oceanogr., 41, 1375–1383, 1996.

Glaser, P. H., Chanton, J. P., Morin, P., Rosenberry, D. O., Siegel, D. I., Ruud, O., Chasar, L. I., and Reeve, A. S.: Surface deformations as indicators of deep ebullition fluxes in a large northern peatland, Global Biogeochem. Cy., 18, GB1003, doi:10.1029/2003GB002069, 2004.

Greene, S., Walter Anthony, K. M., Archer, D., Sepulveda-Jauregui, A., and Martinez-Cruz, K.: Modeling the impediment of methane ebullition bubbles by seasonal lake ice, Biogeosciences, 11, 6791-6811, doi:10.5194/bg-11-6791-2014, 2014.

Grosse, G., Harden, J., Turetsky, M., McGuire, A. D., Camill, P., Tarnocai, C., Frolking, S., Schuur, E. A. G., Jorgenson, T., Marchenko, S., Romanovsky, V., Wickland, K. P., French, N., Waldrop, M., Bourgeau-Chavez, L., and Striegl, R. G.: Vulnerability of high-latitude soil organic carbon in North America to disturbance, J. Geophys. Res., 116, 1–23, doi:10.1029/2010JG001507, 2011.

Grosse, G., Jones, B., and Arp, C.: Thermokarst Lakes, Drainage and Drained Basins, Treatise Geomorphol., 8, 325–353, 2013.

Hinzman, L. D., Bettez, N. D., Bolton, W. R., Chapin, F. S., Dyurgerov, M. B., Fastie, C. L., Griffith, B., Hollister, R. D., Hope, A., Huntington, H. P., Jensen, A. M., Jia, G. J., Jorgenson, T., Kane, D. L., Klein, D. R., Kofinas, G., Lynch, A. H., Lloyd, A. H., Mcguire, A. D., Nelson, F. E., Oechel, W. C., Osterkamp, T. E., Racine, C. H., Romanovsky, V. E., Stone, R. S., Stow, D.

A., Sturm, M., Tweedie, C. E., Vourlitis, G. L., Walker, M. D., Walker, D. A., Webber, P. J., Welker, J. M., and Winker, K. S.: Evidence and Implications of Recent Climate Change in Northern Alaska and Other Arctic Regions, Climatic Change, 72, 251–298, doi:10.1007/s10584-005-5352-2, 2005.

Hugelius, G., Strauss, J., Zubrzycki, S., Harden, J. W., Schuur, E. A. G., Ping, C.-L., Schirrmeister, L., Grosse, G., Michaelson, G. J., Koven, C. D., O'Donnell, J. A., Elberling, B., Mishra, U., Camill, P., Yu, Z., Palmtag, J., and Kuhry, P.: Estimated stocks of circumpolar permafrost carbon with quantified uncertainty ranges and identified data gaps, Biogeosciences, 11, 6573-6593, doi:10.5194/bg-11-6573-2014, 2014.

Jeffries, M. O., Morris, K., and Kozlenko, N.: Ice Characteristics and Remote Sensing of Frozen Rivers and Lakes, Remote Sensing in Northern Hydrology, Geoph. Monog. Series, 163, 63–90, 2005.

Jorgenson, M. T. and Shur, Y.: Evolution of lakes and basins in northern Alaska and discussion of the thaw lake cycle, J. Geophys. Res., 112, 1–12, doi:10.1029/2006JF000531, 2007.

Kanevskiy, M., Shur, Y., Fortier, D., Jorgenson, M. T., and Stephani, E.: Cryostratigraphy of late Pleistocene syngenetic permafrost (yedoma) in northern Alaska, Itkillik River exposure, Quaternary Res., 75, 584–596, doi:10.1016/j.yqres.2010.12.003, 2011.

Keller, M. and Stallard, R. F.: Methane emission by bubbling from Gatun Lake, Panama, J. Geophys. Res., 99, 8307–8319, doi:10.1029/92JD02170, 1994.

Kessler, M. A., Plug, L. J., and Walter Anthony, K. M.: Simulating the decadal- to millennial-scale dynamics of morphology and sequestered carbon mobilization of two thermokarst lakes in NW Alaska, J. Geophys. Res.-Biogeo., 117, 1–22, doi:10.1029/2011JG001796, 2012.

Kokelj, S. V. and Jorgenson, M. T.: Advances in thermokarst research, Permafrost Periglac., 24, 108–119, doi:10.1002/ppp.1779, 2013.

Koven, C. D., Ringeval, B., Friedlingstein, P., Ciais, P., Cadule, P., Khvorostyanov, D., Krinner, G., and Tarnocai, C.: Permafrost carbon-climate feedbacks accelerate global warming, P. Natl. Acad. Sci. USA, 108, 14769–14774, doi:10.1073/pnas.1103910108, 2011.

Lindgren, P. R., Grosse, G., Meyer, F. J., and Walter Anthony, K. M.: Development of an object-based classification model to detect methane ebullition bubbles in early winter lake ice, in preparation, 2015.

Mather, P.: Pattern Recognition Principles In Classification for Remotely Sensed Data, Second Edn., CRC Press, New York, 41–75, 2009.

Mattson, M. D. and Likens, G. E.: Air pressure and methane fluxes, Nature, 347, 718–719, 1990.

Navulur, K.: Multispectral image analysis using the object-oriented paradigm, CRC Press, Boca Raton, FL, 2007.

Péwé, T. L.: Quaternary geology of Alaska, US Geol. Survey Professional Paper 835, 1–145, 1975.

Plug, L. J. and West, J. J.: Thaw lake expansion in a two-dimensional coupled model of heat transfer, thaw subsidence, and mass movement, J. Geophys. Res., 114, F01002, doi:10.1029/2006JF000740, 2009.

Rowland, J. C., Travis, B. J., and Wilson, C. J.: The role of advective heat transport in talik development beneath lakes and

ponds in discontinuous permafrost, Geophys. Res. Lett., 38, 1–5, doi:10.1029/2011GL048497, 2011.

Scandella, B. P., Varadharajan, C., Hemond, H. F., Ruppel, C., and Juanes, R.: A conduit dilation model of methane venting from lake sediments, Geophys. Res. Lett., 38, 1–6, doi:10.1029/2011GL046768, 2011.

Schuur, E. A. G., Bockenheim, J., Canadell, J. P., Euskirchen, E., Field, C. B., Goryachkin, S. V., Hagemann, S., Kuhry, P., Lafleur, P. M., Lee, H., Mazhitova, G., Nelson, F. E., Rinke, A., Romanovsky, V. E., Shiklomanov, N., Tarnocai, C., Venevsky, S., Vogel, J. G., and Zimov, S. A.: Vulnerability of permafrost carbon to climate change: implications for the global carbon cycle, BioScience, 58, 701–714, doi:10.1641/B580807, 2008.

Smith, L. C., Sheng, Y., and MacDonald, G. M.: A first pan-Arctic assessment of the influence of glaciation, permafrost, topography and peatlands on northern hemisphere lake distribution, Permafrost Periglac., 18, 201–208, 2007.

Tokida, T., Miyazaki, T., and Mizoguchi, M.: Ebullition of methane from peat with falling atmospheric pressure, Geophys. Res. Lett., 32, L13823 doi:10.1029/2005GL022949, 2005.

Varadharajan, C.: Magnitude and spatio-temporal variability of methane emissions from a eutrophic freshwater lake, PhD thesis, Massachusetts Institute of Technology, Cambridge, MA, 2009.

Walter, K. M., Zimov, S. A., Chanton, J. P., Verbyla, D., and Chapin, F. S.: Methane bubbling from Siberian thaw lakes as a positive feedback to climate warming, Nature, 443, 71–75, doi:10.1038/nature05040, 2006.

Walter, K. M., Smith, L. C., and Chapin, F. S.: Methane bubbling from northern lakes: present and future contributions to the global methane budget, Philos. T. R. Soc. A, 365, 1657–1676, doi:10.1098/rsta.2007.2036, 2007.

Walter, K. M., Engram, M., Duguay, C. R., Jeffries, M. O., and Chapin, F. S.: The potential use of Synthetic Aperture Radar for estimating methane ebullition from Arctic lakes, J. Am. Water Resour. As., 44, 305–315, 2008.

Walter Anthony, K., Vas, D. A., Brosius, L., Chapin III, F. S., and Zimov, S. A.: Estimating methane emissions from northern lakes using ice- bubble surveys, Limnol. Oceanogr.-Meth., 8, 592–609, 2010.

Walter Anthony, K. M. and Anthony, P.: Constraining spatial variability of methane ebullition seeps in thermokarst lakes using point process models, J. Geophys. Res.-Biogeo., 118, 1–20, doi:10.1002/jgrg.20087, 2013.

Walter Anthony, K. M., Anthony, P., Grosse, G., and Chanton, J.: Geologic methane seeps along boundaries of Arctic permafrost thaw and melting glaciers, Nat. Geosci., 5, 419–426, doi:10.1038/ngeo1480, 2012.

Walter Anthony, K. M., Zimov, S. A., Grosse, G., Jones, M. C., Anthony, P., Chapin III, F. S., Finlay, J. C., Mack, M. C., Davydov, S., Frenzel, P., and Frolking, S.: A shift of thermokarst lakes from carbon sources to sinks during the Holocene epoch, Nature, 511, 452–456, doi:10.1038/nature13560, 2014.

West, J. J. and Plug, L. J.: Time-dependent morphology of thaw lakes and taliks in deep and shallow ground ice, J. Geophys. Res., 113, 1–14, doi:10.1029/2006JF000696, 2008.

Wik, M., Crill, P. M., Bastvikenm D., Danielsson, Å., and Norbäck, E.: Bubbles trapped in arctic lake ice: Potential implications for methane emissions, J. Geophys. Res., 116, 1–10, doi:10.1029/2011JG001761, 2011.

Zimov, S. A., Voropaev, Y. V., Semiletov, I. P., Davidov, S. P., Prosiannikov, S. F., Chapin III, F. S., Chapin, M. C., Trumbore, S., and Tyler, S.: North Siberian Lakes: A methane source fueled by Pleistocene carbon, Science, 277, 800–802, doi:10.1126/science.277.5327.800, 1997.

Zimov, S. A., Davydov, S. P., Zimova, G. M., Davydova, A. I., Schuur, E. A. G., Dutta, K., and Chapin III, F. S.: Permafrost carbon: Stock and decomposability of a globally significant carbon pool, Geophys. Res. Lett., 33, , 1–5, doi:10.1029/2006GL027484, 2006.